

ARTICLE TYPE

Evaluating the accuracy of the actuator line model against blade element momentum theory in uniform inflow

Luoqin Liu^{1,2} | Lucas Franceschini³ | Daniel F. Oliveira⁴ | Flavio C. C. Galeazzo⁵ | Bruno S. Carmo³ | Richard J. A. M. Stevens^{*2}

¹Department of Modern Mechanics, University of Science and Technology of China, Hefei 230026, Anhui, PR China

²Physics of Fluids Group, Max Planck Center Twente for Complex Fluid Dynamics, University of Twente, 7500 AE Enschede, The Netherlands

³Department of Mechanical Engineering, Escola Politécnica, University of São Paulo, São Paulo, SP 05508-030, Brazil

⁴Department of Naval Architecture & Ocean Engineering, Escola Politécnica, University of São Paulo, São Paulo, SP 05508-030, Brazil

⁵High Performance Computing Center Stuttgart (HLRS), Nobelstr. 19, 70569 Stuttgart, Germany

Correspondence

*Richard J. A. M. Stevens, Physics of Fluids Group, Max Planck Center Twente for Complex Fluid Dynamics, University of Twente, 7500 AE Enschede, The Netherlands.

Email: r.j.a.m.stevens@utwente.nl

Abstract

We evaluate the accuracy of the actuator line model (ALM) approach by performing simulations for the NREL 5 MW wind turbine in uniform inflow using three large eddy simulation codes. The power and thrust coefficients obtained using the three codes agrees within 1% when the grid spacing $\Delta_{\text{grid}} \leq 5.25$ m, and are cross-validated against blade element momentum (BEM) theory. We find that the results of ALM converge towards BEM theory without the need for tip correction when the numerical resolution is increased. For $\Delta_{\text{grid}} = 0.98$ m the difference between the power and thrust coefficient obtained using ALM and BEM is 4.5% and 2.1%, respectively, although we note that no absolute convergence between ALM and BEM can be obtained as both models use different assumptions, such as the use of a force projection method in the ALM. The difference in the local axial and tangential forces along the blades obtained from ALM simulations using $\Delta_{\text{grid}} = 1.97$ m and $\Delta_{\text{grid}} = 0.98$ m can be as large as 10%. The effect of the number of actuator points on the obtained turbine power and thrust coefficients is limited as the results converge when the spacing between the actuator points is about three times the grid spacing. This insight on the required number of blade points can be used to improve the efficiency of actuator line simulations.

KEYWORDS:

Actuator line model, blade element momentum, large eddy simulation

1 Introduction

Wind-turbine performance assessment and design are routinely performed using blade element momentum (BEM) theory¹. This method is a combination of the momentum theory introduced by Rankine² from a macroscopic point of view and the blade element theory introduced by Froude³ from a local point of view. A basic assumption of the method is that half of the induction is over the rotor plane. Furthermore, the analysis assumes that the flow around the different blade sections is independent. The aerodynamic forces are obtained using tabulated aerofoil data derived from wind tunnel measurements or numerical simulations and corrected for three-dimensional effects⁴. However, owing to the limitations to represent various flow situations encountered in practice, it has become necessary to introduce different empirical corrections. Such situations include dynamic inflow, yaw misalignment, tip loss corrections, and heavily loaded rotors⁵. Although BEM is sometimes referred to as a “low-fidelity” model, it should be noted that the BEM theory generates reliable results for rotors operating close to their design conditions and can therefore be used as a reliable reference when experimental data is not available⁶.

Large eddy simulations (LES) have become a prominent tool for performing high-fidelity simulations of wind turbine wakes and wind farm flows^{7,8,9,10,11}. LES can capture the three-dimensional unsteady character of the flow around wind turbines and evaluate the wind turbine performance. However, even with modern supercomputers, it is very challenging to fully resolve the flow around the blades in LES, and this requires the use of body-fitted meshes, see Refs.^{12,13,14}. As the use of body-fitted meshes is not yet practical for wind farm simulations, the actuator line model (ALM) is widely used to model wind turbines. The ALM is based on the blade element theory using tabulated aerofoil data with the velocities computed from computational fluid dynamics (CFD)^{4,15,16,7,17,18,19,20,21,22}.

The ALM was originally developed for horizontal axis wind turbines by Sørensen and Shen⁴ and has later been extended to vertical axis wind turbines²³. In the ALM the forces on the blades, which are discretized as rotating lines of actuator points, are calculated using tabulated airfoil data based on the local angle of attack at the location of the actuator point at each time step of the calculation. Subsequently, the forces are projected from the actuator points to the flow solver to ensure the effect of the rotating blades is evaluated by the flow solver. Typically this force projection is performed using an isotropic Gaussian function⁴, although the use of non-isotropic Gaussian kernel function, in which the force projection width is different in each direction, has been proposed to represent the shape of the blades more accurately^{24,25,10,26}. Shives and Crawford²⁰ suggested that the spreading parameter ϵ should be related to the local chord length c , namely as $c/8 \leq \epsilon \leq c/4$, for elliptical loaded wings. By minimizing the error between the potential flow around a two-dimensional airfoil and the flow generated by a Gaussian distributed body force Martínez-Tossas et al²⁵ concluded that $\epsilon = 0.2c$ should be employed for a low angle of attack. Later, Rocchio et al²⁷ found that at a high angle of attack potential flow theory is not appropriate as flow separation occurs, and the optimal value is $\epsilon \approx 0.1c$. Note that the highest resolution used in the present study is $\epsilon = 0.7\bar{c}$ (case G in Table 1), where $\bar{c} = 3.5$ m is the mean chord length of the blade. Therefore, in this work, we will not consider these aspects as even on modern supercomputers, the resolution of LES calculations is too limited to satisfy these conditions for wind farm simulations. Instead, we focus on a detailed analysis of the ALM accuracy in its *traditional* form to give more detailed analysis, insights, and guidelines of its accuracy for grid resolution employed in realistic, high-fidelity simulations of wind turbine wakes and wind farm flows.

This study considers the well-known National Renewable Energy Laboratory (NREL) 5 MW wind turbine, which was developed by Jonkman et al.²⁸, to provide a representative utility-scale reference turbine. This turbine has a rotor diameter of $D = 126$ m, and the three blades are defined using the cross-sectional Delft University and National Advisory Committee for Aeronautics profiles since their aerodynamic properties are well known and are further extended to high angles of attack²⁹ and corrected for three-dimensional rotational effects³⁰, see also Ning³¹. The obtained accuracy of the ALM model depends on the width of force projection compared to the grid spacing Δ_{grid} and the spacing between the actuator points along the blade Δ_{blade} . It is well-known that the force projection ϵ needs to be sufficiently large to suppress numerical instabilities, while a large ϵ leads to inaccurate force distributions^{7,32,21,33}. It is typically recommended to set $\epsilon \geq 2\Delta_{\text{grid}}$ ^{7,33}. Jha et al.²¹ proposed to use a grid resolution of $D/\Delta_{\text{grid}} = [60, 120]$ in combination with $D/\Delta_{\text{blade}} \geq 40$ to accurately capture the rotor thrust and power. In addition, they recommended that the actuator points should be chosen such that $\Delta_{\text{blade}} \approx 1.5\Delta_{\text{grid}}$.

In this work, we reevaluate these guidelines by comparing three LES codes with BEM theory. In agreement with previous work, we find that D/Δ_{grid} needs to be sufficiently high to get accurate results, in particular to get accurately capture the local forces along the blades. However, as a refinement of previous results, we will show that the number of actuator points is less important to capture the turbine's thrust and power accurately. It is shown that using $\Delta_{\text{blade}} \leq 3\Delta_{\text{grid}}$ does not significantly improve the quality of the result. This indicates that the number of actuator points can be reduced compared to previous guidelines with *limited* loss of accuracy. This can be relevant when the ALM is employed in large-scale computations in which the ALM calculations, which are local in space, may result in significant computational overhead. The remainder of this paper is organized as follows. In section 2 we introduce the technical details of the ALM briefly. Section 3 introduces the numerical codes, and the main results and findings are presented in section 4. The conclusions are summarized in section 5.

2 Actuator line model

The turbine blades in the ALM are represented by distributed body forces on the quarter-chord lines of the blades. The velocity field is solved in a global coordinate system (x, y, z) in streamwise, cross-stream, and vertical directions. The angle θ defines the azimuthal position of one of the blades, with the blades located at an angle $\Delta\theta = 2\pi/B$ from each other, where B is the number of the blades ($B = 3$ for the NREL 5 MW turbine considered in this study). A local, rotating coordinate system (r, θ, x) , as seen from the rotor blade, is used to determine the relative velocity. The lift and drag forces are calculated dynamically using the local velocity at each actuator point using tabulated drag and lift coefficients.

Denoting (u_x, u_y, u_z) the interpolated velocity on the actuator line points, Ω the rotor rotational speed, r is the radius at the actuator line point, the local relative azimuthal velocity u_θ of the blade is then given as

$$u_\theta = \Omega r - u_y \cos \theta + u_z \sin \theta. \quad (1)$$

The angle of attack α for each actuator point is given by

$$\alpha = \phi - \gamma, \quad \phi = \arctan\left(\frac{u_x}{u_\theta}\right), \quad (2)$$

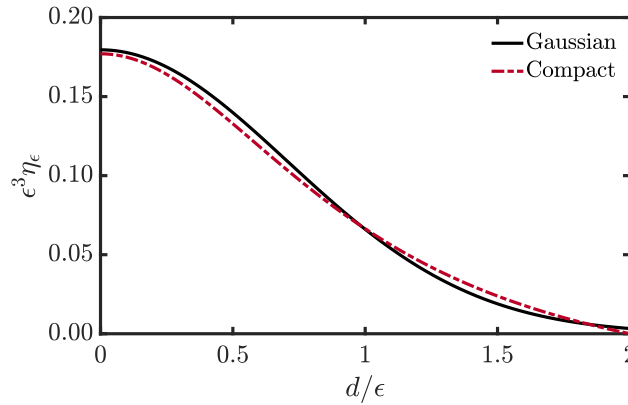


FIGURE 1 Comparison of the Gaussian kernel function (5) and the compact kernel function (7)

where γ accounts for the local twist and pitch angle of the blade. The lift and drag forces per unit span are obtained using

$$f_L = \frac{1}{2} \rho u_{\text{rel}}^2 c C_l, \quad f_D = \frac{1}{2} \rho u_{\text{rel}}^2 c C_d, \quad (3)$$

where ρ is the density of fluid, $u_{\text{rel}} = \sqrt{u_\theta^2 + u_x^2}$ is the local wind velocity relative to the blade, c is the local chord length, and C_l and C_d are the local lift and drag coefficients corrected for three-dimensional effects, respectively. The forces are transferred from the rotor frame to the global coordinate frame as follows

$$f_x = -(f_L \cos \phi + f_D \sin \phi), \quad f_y = -(f_L \sin \phi - f_D \cos \phi) \cos \theta, \quad f_z = (f_L \sin \phi - f_D \cos \phi) \sin \theta. \quad (4)$$

To avoid numerical instabilities caused by the turbine forces it is common to use a Gaussian force projection method³⁴,

$$\eta_\epsilon = \frac{1}{\epsilon^3 \pi^{3/2}} e^{-d^2/\epsilon^2}, \quad (5)$$

with

$$d = \sqrt{(x_{i,j,k} - x^a)^2 + (y_{i,j,k} - y^a)^2 + (z_{i,j,k} - z^a)^2}. \quad (6)$$

Here, the indices i, j, k refer to the streamwise, spanwise, and vertical grid indices in the global coordinate frame, the superscript a indicates the actuator line point index, and ϵ establishes the width of the force projection kernel. Based on the recommendation by Martínez-Tossas *et al.*³³, we set $\epsilon = 2.5 \Delta_{\text{grid}}$ throughout the entire study.

One downside of the Gaussian force projection method is that it goes to zero very slowly. This means that the region over which the force projection is calculated should be either truncated and the results normalized afterwards, or the calculation becomes very inefficient as the convolution is calculated over a very large region. A way to avoid this is to use the following compact force projection function

$$\eta_\epsilon = \frac{a}{4\pi\epsilon^3} \frac{4 - (d/\epsilon)^2}{1 + (d/\epsilon)^2} H(2 - d/\epsilon), \quad a = \frac{3}{22 - 15 \arctan 2}, \quad (7)$$

where H is the Heaviside function,

$$H(x) = 0, \quad x < 0; \quad H(x) = 1, \quad x > 0. \quad (8)$$

It is shown in figure 1 that this force projection function is very similar to the Gaussian projection function, which means that both force projection methods should essentially give the same result. The results presented below confirm this. This force projection method is conservative over a distance of $2d/\epsilon$. This can provide computation benefits as the force projection radius that must be considered is confined and prevents the need to renormalize the results to account for small truncation errors required using the Gaussian projection method.

3 Brief overview codes

In LES the spatially-filtered Navier-Stokes equations:

$$\partial_t \tilde{\mathbf{u}} + \tilde{\mathbf{u}} \cdot \nabla \tilde{\mathbf{u}} = \mathbf{f}_{\text{wt}} - \nabla \tilde{p} - \nabla \cdot \boldsymbol{\tau}, \quad \nabla \cdot \tilde{\mathbf{u}} = 0, \quad (9)$$

where $\tilde{\mathbf{u}}$ is the velocity, \mathbf{f}_{wt} is the force due to the wind turbine obtained using the ALM model described above, \tilde{p} is the modified pressure, and $\boldsymbol{\tau}$ is the deviatoric part of the sub-grid scale shear stress, which is modeled as

$$\boldsymbol{\tau} = -2\nu_t \tilde{\mathbf{S}}, \quad \nu_t = (C_s \Delta_{\text{grid}})^2 \sqrt{2\tilde{\mathbf{S}} : \tilde{\mathbf{S}}}, \quad \tilde{\mathbf{S}} \equiv \frac{1}{2} [\nabla \tilde{\mathbf{u}} + (\nabla \tilde{\mathbf{u}})^T]. \quad (10)$$

Here the superscript T denotes a matrix transpose, $\Delta_{\text{grid}} = (\Delta x \Delta y \Delta z)^{1/3}$ is the grid scale with Δx , Δy , Δz the grid spacings in the streamwise (x), spanwise (y) and vertical (z) directions, respectively. All presented simulations are performed using the standard Smagorinsky model with $C_s = 0.16$ ³⁵. Note that this value, as well as the turbulence model, has limited influence on the load distributions³³.

The airfoil data²⁸ is given at blade locations directed along the blade axis with coordinates at the midpoint of each blade element. The blade length and its root and tip locations are calculated using this information. Using the input parameters from Jonkman *et al.*²⁸, the total length of the wind turbine blades reported by WInc3D and turbinesFoam is smaller than the assumed 63 m due to the method that is used to calculate the blade element locations. The blade length is a relevant value, as a slightly shorter blade implies calculating the forces to be underpredicted. Both codes have been modified to account for this.

3.1 Pseudo-spectral LES solver

At the University of Twente we develop a pseudo-spectral LES code^{36,37} that is related to the LESGO code, which originates from the work by Albertson³⁸, and later contributions by Bou-Zeid *et al.*³⁹, Meyers and Meneveau⁴⁰, Calaf *et al.*⁴¹, and Stevens *et al.*⁴², Martínez-Tossas *et al.*^{33,9}. The computational grids are uniformly distributed in the horizontal directions and are staggered in the vertical direction. The first vertical velocity grid plane is located at the ground, while the first horizontal velocity grid planes are located at half grid distance above the ground. The code is pseudo-spectral, implying periodic boundary conditions in the streamwise and spanwise directions. The vertical direction uses the second-order centered finite difference method. The boundary conditions in this direction are zero shear stress with no penetration. Time integration is done using the second-order Adams-Bashforth method.

3.2 WInc3D

WInc3D⁴³ provides an integrated wind farm simulation framework that allows detailed analyses of wake-wake and turbine-wake interactions. The code is based on higher-order compact finite-difference discretization schemes⁴⁴ and uses an efficient 2D domain decomposition algorithm that allows the code to scale up to $O(10^5)$ computational cores⁴⁵. The pressure mesh is staggered from the velocity one by half a mesh to avoid spurious pressure oscillations. An explicit third-order Adams-Bashforth time advancement scheme is used for time marching. WInc3D offers several built-in models, including a native ALM that has been validated by comparisons with experiments^{46,47,43}.

3.3 turbinesFoam

OpenFOAM⁴⁸ is an open-source CFD toolbox, which coupled with the ALM library turbinesFoam^{49,50} allows the simulation of wind and marine hydrokinetic turbines. Functions such as interpolation, Gaussian projection, and vector rotation were adapted from NREL's SOWFA⁵¹. The flow code is based on the finite volume method, with second-order accuracy in space and time. turbinesFoam has been validated for wind aligned and yawed tandem wind turbines⁵².

4 Actuator line model results for NREL 5 MW in uniform inflow

We performed simulations for the NREL 5 MW reference wind turbine²⁸ subject to non-turbulent uniform inflow condition of $U_\infty = 8$ m/s, and no pressure gradient applied. The rotational speed of the rotor was fixed at $\Omega = 9.1552$ RPM, giving a tip speed ratio of $\Lambda = 7.55$. These conditions were chosen to provide the turbine's optimum power coefficient, extracting maximum energy from the flow. All simulations were performed in a $L_x \times L_y \times L_z = 8D \times 6D \times 6D$ domain in streamwise, spanwise and vertical directions, respectively. For simplicity, we used a uniform grid in all directions. The turbine was located at $3D$ downstream of the inlet in the middle of the y - z plane. We used periodic boundary conditions in the spanwise direction and stress-free conditions in the vertical direction. The fringe region at the end of the domain was 7.5% of the streamwise domain length⁴². The results presented in this paper were obtained after the simulation reached its statistically stationary state. This test case was also used in previous validation studies; see e.g. Jha *et al.*²¹, Martínez Tossas *et al.*³³, Churchfield *et al.*²⁴, and Dağ and Sørensen⁶.

4.1 Blade element momentum analysis

As the NREL 5 MW wind turbine is idealized such that there is no experimental data to compare with, we compare the LES results using the ALM with the theoretical predictions from BEM theory^{1,5}. For each blade element, the aerodynamic forces, similar to the ALM, are obtained using tabulated airfoil data, which are assumed to be corrected for three-dimensional effects^{34,28}. We assume that the blade loading is not very heavy such that additional correction for the thrust coefficient is not required⁵³. Thus, the BEM analysis gives the following closed system^{54,5},

$$\tan \phi = \frac{1 - a}{\lambda(1 + a')}, \quad \frac{a}{1 - a} = \frac{\sigma C_n(\phi)}{4 \sin^2 \phi}, \quad \frac{a'}{1 - a} = \frac{\sigma C_t(\phi)}{4 \lambda \sin^2 \phi}. \quad (11)$$

Here ϕ is the relative angle, a and a' are the axial and tangential induction factors, $\lambda = \Omega r / U_\infty$ is the local speed ratio, $\sigma = Bc / (2\pi r)$ is the solidity of the turbine, and

$$C_n(\phi) = C_l(\alpha) \cos \phi + C_d(\alpha) \sin \phi, \quad C_t(\phi) = C_l(\alpha) \sin \phi - C_d(\alpha) \cos \phi \quad (12)$$

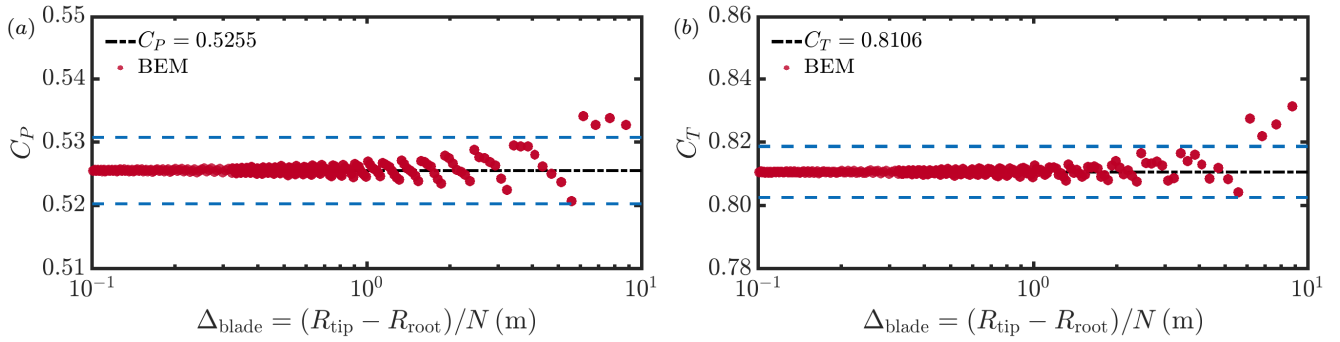


FIGURE 2 The (a) power C_P and (b) thrust C_T coefficient obtained using BEM theory as function of the distance between the actuator points Δ_{blade} . The dashed-dotted black line indicates the high-resolution limit obtained using $N = 1024$ actuator points. The dashed blue lines indicate the 1% relative error, which is obtained for $N \geq 13$.

TABLE 1 Comparison of power C_P and thrust C_T coefficients obtained in the UTwente-LES simulations with the Gaussian and compact force projection methods. The columns from left to right indicate the case name, the used numerical resolution in the streamwise, spanwise, and vertical direction ($N_x \times N_y \times N_z$), the grid spacing Δ_{grid} . The number of actuator points along each blade is $N = N_y/3$. The $C_{P,g}$ and $C_{T,g}$ are obtained using the Gaussian projection function (Eq. (5)) and $C_{P,c}$ and $C_{T,c}$ using the compact projection function (Eq. (7)).

Case	$N_x \times N_y \times N_z$	Δ_{grid} (m)	$C_{P,g}$	$C_{P,c}$	$C_{T,g}$	$C_{T,c}$
A	128 × 96 × 96	7.88	0.6034	0.6002	0.8542	0.8521
B	192 × 144 × 144	5.25	0.6077	0.6051	0.8618	0.8602
C	256 × 192 × 192	3.94	0.5891	0.5868	0.8521	0.8505
D	384 × 288 × 288	2.63	0.5745	0.5727	0.8444	0.8433
E	512 × 384 × 384	1.97	0.5650	0.5633	0.8379	0.8368
F	768 × 576 × 576	1.31	0.5547	0.5531	0.8313	0.8302
G	1024 × 768 × 768	0.98	0.5494	0.5479	0.8280	0.8270

are the normal and tangential force coefficients, respectively, where $\alpha = \phi - \gamma$ is the local angle of attack and γ is the blade twist angle, and C_l and C_d are the corrected lift and drag coefficients. The closed system (ϕ, a, a') can be solved by an iterative method^{54,5}, of which the existence and uniqueness have been proved mathematically by Ledoux *et al.*⁵⁵. Subsequently, the axial and tangential forces per unit span along each blade can be obtained

$$F_n = \frac{1}{2} \rho U_\infty^2 C_n c \left(\frac{1-a}{\sin \phi} \right)^2, \quad F_t = \frac{1}{2} \rho U_\infty^2 C_t c \left(\frac{1-a}{\sin \phi} \right)^2. \quad (13)$$

Finally, the total thrust T and power output P of the wind turbine can be obtained by integrating these forces along the three turbine blades as follows

$$T = \frac{3}{2} \rho U_\infty^2 \int C_n c \left(\frac{1-a}{\sin \phi} \right)^2 dr, \quad P = \frac{3}{2} \rho U_\infty^2 \Omega \int C_t c \left(\frac{1-a}{\sin \phi} \right)^2 r dr. \quad (14)$$

Figure 2 shows the power coefficient $C_P = 8P/(\rho U_\infty^3 \pi D^2)$ and the thrust coefficient $C_T = 8T/(\rho U_\infty^2 \pi D^2)$ obtained using BEM theory as function of the distance between the actuator points $\Delta_{\text{blade}} = (R_{\text{tip}} - R_{\text{root}})/N$, where N is the number of actuator points along each blade. The figure shows that the C_P and C_T values obtained using $\Delta_{\text{blade}} \leq 4.7$ m, which corresponds to the use of $N \geq 13$ actuator points along each blade, agree within 1% with the high-resolution limit obtained by $N = 1024$.

4.2 Effect of the force projection function

Here we present a comparison of the results obtained using different methods to account for the presence of actuator points in the flow, namely, the Gaussian force projection method, Eq. (5), and the compact force projection function, Eq. (7). From the comparison between the two force functions presented in figure 1, we did not expect significant differences in the C_P and C_T results obtained with either approach and table 1 shows this is what indeed happens. In particular, table 1 shows that the newly proposed force projection method gives essentially the same results (the <1% difference is less than other uncertainties) as the commonly employed Gaussian force projection method. Hence all the findings obtained for the Gaussian force projection method extend to the newly introduced force projection.

TABLE 2 Comparison of power C_P and thrust C_T coefficients obtained in the pseudo-spectral LES solver (UT), Winc3D (W3D) and turbinesFoam (TF) simulations. The columns from left to right indicate the case name, the used numerical resolution in the streamwise, spanwise, and vertical direction ($N_x \times N_y \times N_z$), and the grid spacing Δ_{grid} . The number of actuator points along each blade is $N = N_y/3$. The C_P and C_T are obtained using the Gaussian projection function (Eq. (5)).

Case	$N_x \times N_y \times N_z$	Δ_{grid} (m)	C_P^{UT}	C_P^{W3D}	C_P^{TF}	C_T^{UT}	C_T^{W3D}	C_T^{TF}
A	128 × 96 × 96	7.88	0.6034	0.6365	0.6355	0.8542	0.8777	0.8764
B	192 × 144 × 144	5.25	0.6077	0.6032	0.6017	0.8618	0.8584	0.8569
C	256 × 192 × 192	3.94	0.5891	0.5883	0.5882	0.8521	0.8514	0.8507
D	384 × 288 × 288	2.63	0.5745	0.5745	0.5717	0.8444	0.8444	0.8415
E	512 × 384 × 384	1.97	0.5650	0.5655	0.5619	0.8379	0.8382	0.8343
F	768 × 576 × 576	1.31	0.5547	0.5532	0.5523	0.8313	0.8304	0.8272
G	1024 × 768 × 768	0.98	0.5494	-	-	0.8280	-	-

The data in table 1 were calculated with the pseudo-spectral LES solver, but we also ran tests using Winc3D, which also demonstrated that the differences are minimal, thus confirming our findings. So this shows that the computational performance of ALM codes can possibly be improved by using this alternative formulation, since the operations are cheaper than the traditional Gaussian projection approach, without any noticeable change in the results within a tolerance of less than 1%. We remark that the computation benefit of the new force projection is expected to depend on the considered case, for example, on the number of turbines compared to the considered volume and the used simulation code. In the present test case, we consider only one turbine, and therefore the benefit of the proposed force projection method is limited (a few percentage points) as the relative computational requirements for the ALM calculations are limited for this case. In any case, we note that reducing the number of actuator blade points, as suggested by our findings below, is a more effective way to reduce the computational overhead of the ALM calculations. However, a benefit of the compact function is that no truncation is required, preventing small fluctuations in time-dependent forces as the blades move through the grid.

4.3 Effect of the LES grid spacing

In this section, we analyze the effect of the grid resolution by varying the number of grid points $N_x \times N_y \times N_z$ in the streamwise, spanwise, and vertical directions, respectively. We ensured that the grid resolution in each direction is the same. The number of actuator points along each blade is $N = N_y/3$. The results are summarized in table 2 and figures 3 and 4. The figures compare the axial F_n and tangential F_t per unit span along each blade as a function of the employed grid resolution with high-resolution BEM result obtained using $N = 1024$ actuator points. The figure shows that both the axial and tangential forces obtained in the simulations converge towards the BEM results when the resolution of the simulations is increased. Difference between ALM and BEM are observed at the locations where the blade changes abruptly from one airfoil type to another. These discontinuities are most noticeable in the tangential force obtained at lower grid resolutions (Fig. 3b,d,f). Figure 5 shows the relative error, defined by the ratio of the results obtained by lower resolution cases (A-F) and the highest resolution case G, of (a) axial and (b) tangential force per unit span along the blade using the pseudo-spectral LES solver. Because the axial force at $r/R \leq 0.16$ is negligibly small; the corresponding relative error is defined as zero in figure 5(a). The figure reveals that the distribution of the forces along the blades obtained using ALM converge towards the BEM results when the numerical resolution is increased. However, it is essential to note that the local blade forces obtained using an ~ 2 m resolution and a ~ 1 m resolution can be as high as 10%, see the tangential forces in figure 5(a), which indicates that a high resolution is required to capture the local forces on the blades accurately. We also note that both the axial and tangential forces in most of the middle part of the blade are slightly above the BEM results. This is in agreement with the finding that the total thrust and power output obtained by the ALM simulations are slightly above the BEM theory for the employed grid resolutions, see table 2.

Figure 6 shows the dependence of the thrust C_T and power C_P coefficient on the employed grid spacing Δ_{grid} . In agreement with the results presented in the table 2, the figure shows that the results obtained using the three codes agree very well. In particular, for $\Delta_{\text{grid}} \leq 5.25$ m the difference is always less than 1%. However, for the coarsest mesh $\Delta_{\text{grid}} = 7.88$ m a difference of about 6% is observed. We speculate that the differences on this coarsest mesh, which is equivalent to about 8 points per blade length and thus much coarser than what is generally considered acceptable for ALM simulations^{56,57}, are due to differences in the employed numerical methods in the three codes. Furthermore, we note the difference in the thrust and power coefficients between the two highest resolution simulations, i.e. F ($\Delta_{\text{grid}} \leq 1.31$ m) and G ($\Delta_{\text{grid}} \leq 0.98$ m) cases, is less than 1%, while the difference between the highest resolution case G and the BEM prediction is 4.5% for the power coefficient and

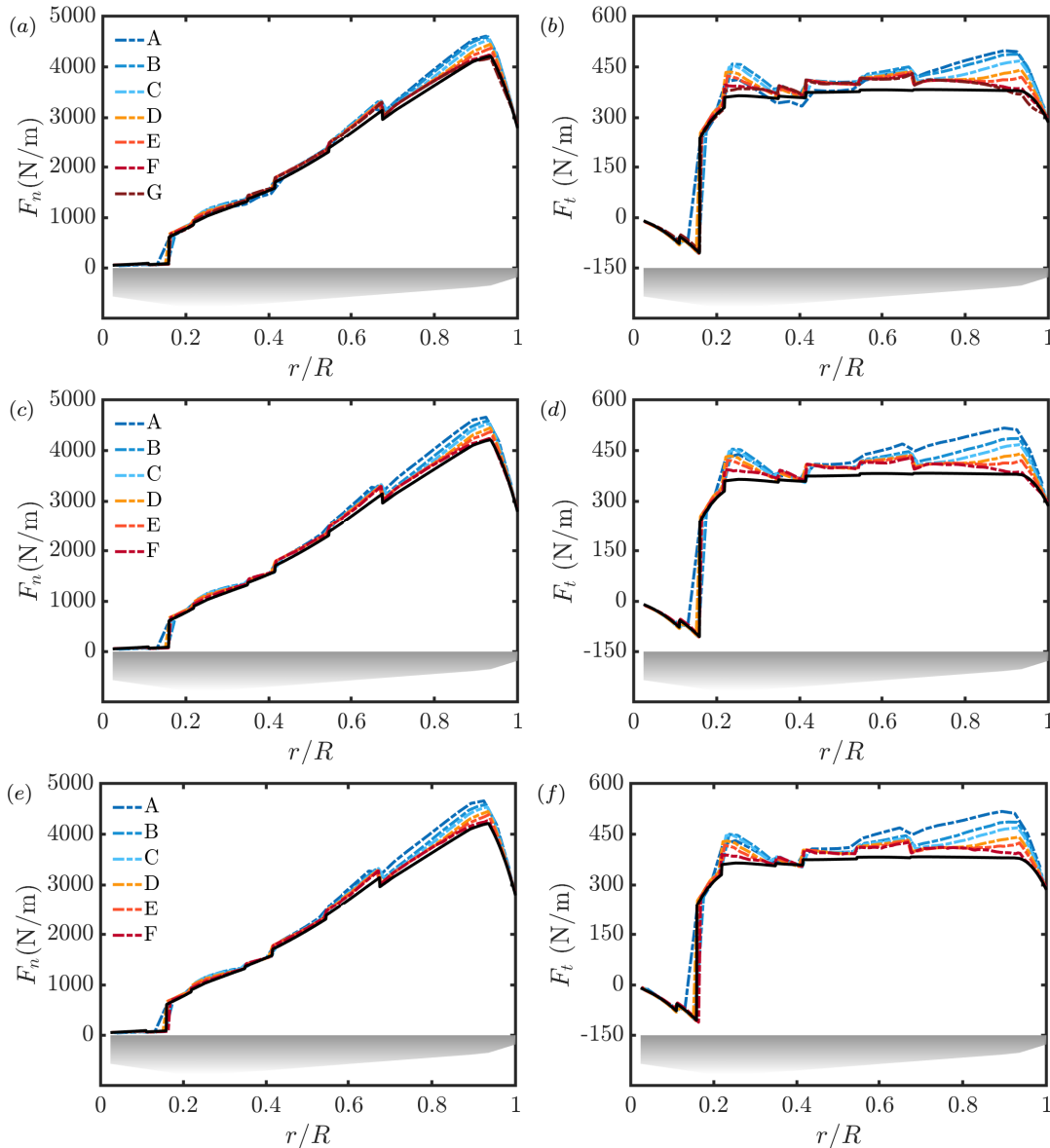


FIGURE 3 The (a,c,e) axial and (b,d,f) tangential force per unit span along the blade obtained in the pseudo-spectral LES solver (a,b), Winc3D (c,d), and turbinesFoam (e,f) simulations. The solid line indicates the high-resolution ($N = 1024$) BEM reference results and the symbols indicate the simulation results obtained on different grid resolutions, see table 2 for details.

2.1% for the thrust coefficient (see table 2). The power and thrust coefficients in the ALM model are higher than in BEM because the blade forces on coarser meshes are more spread out due to which the wind velocity and forces on the blade are higher at the blade location than on a finer mesh. Therefore, the axial and tangential forces are slightly above the BEM results (see figures 3 and 4).

It is worth mentioning that the obtained LES results are not strictly speaking convergent to the BEM results, even though the difference becomes smaller when the grid resolution increases. For example, the value of C_T obtained by LES with the highest resolution (case G) is about 2.1% larger than the BEM prediction. The physical interpretation of the root cause of these discrepancies lies in the intrinsic difference between BEM and LES. Relevant in the present context are assumptions in BEM theory that each annular ring is independent of every other annular ring and that there is no wake expansion, while these effects are automatically accounted for in LES. On the other hand, ALM in LES uses a force projection method not used in BEM. As $\epsilon = 2.5\Delta_{\text{grid}}$ the force projection radius changes with increasing resolution. This means that with increasing grid resolution, the physical problem changes. This is why no absolute convergence of the ALM results is obtained with increasing grid resolution.

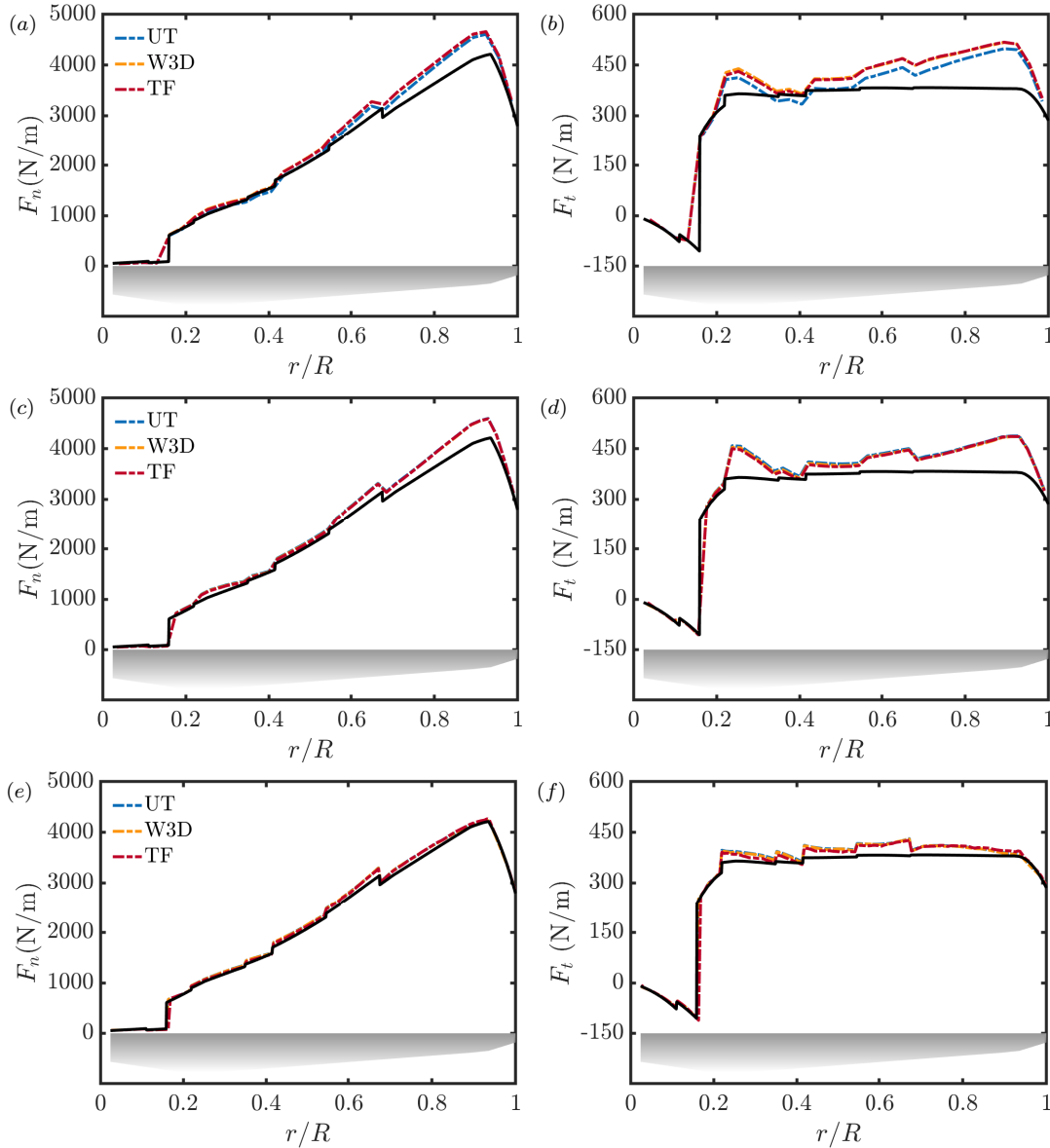


FIGURE 4 The (a,c,e) axial and (b,d,f) tangential force per unit span along the blade obtained in the pseudo-spectral LES solver (UT), Winc3D (W3D), and turbinesFoam (TF) simulations for case A (a,b), B (c,d), and F (e,f). The solid line indicates the high-resolution ($N = 1024$) BEM reference results and the symbols indicate the simulation results obtained on different grid resolutions, see table 2 for details.

4.4 Effect of the number of actuator points

The BEM analysis in section 4.1 revealed that a limited number of actuator points per blade already allows one to calculate the power and thrust coefficients reasonably accurately. To assess whether this conclusion also holds for a practically implemented ALM model, we systematically vary the number of actuator points as indicated in table 3 while keeping the grid resolution constant at $\Delta_{\text{grid}} = 1.31$ m. Figure 7 shows that C_T and C_P converge towards the high resolution result obtained on this grid resolution when the distance between the actuator points is $\Delta_{\text{blade}} \leq 4.1$ m. Figure 8 confirms that the axial and tangential force per unit span along each blade is captured well, even when the number of actuator points is limited. The convergence around ~ 4 m corresponds to about three times the grid spacing, which corresponds to the region over which most of the force projection takes place, i.e. $d/\epsilon \leq 1.5$ in figure 1 on either side of the actuator point. Essentially, this result shows that it is mainly the resolution of the CFD grid Δ_{grid} that determines the accuracy of the ALM results and that the spacing between the actuator points, or in other words, the number of actuator points per blade, has a limited effect on the accuracy of the power and thrust obtained from the ALM calculations.

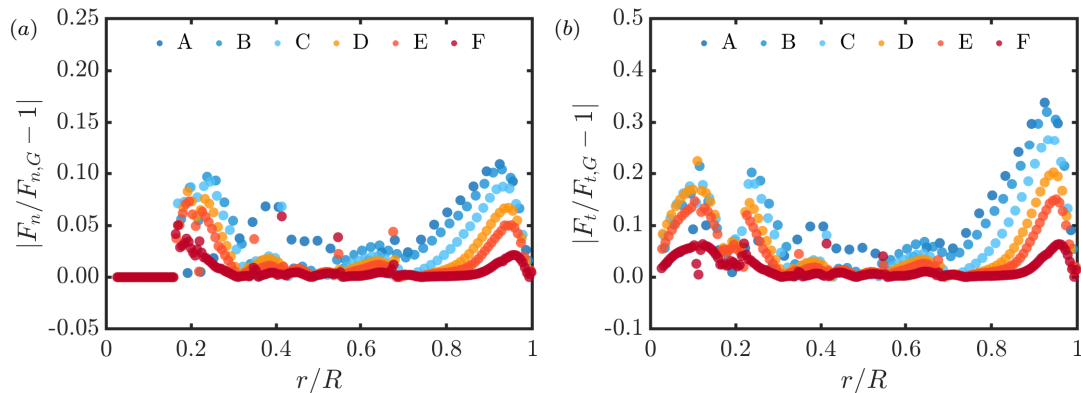


FIGURE 5 The relative error of (a) axial and (b) tangential force per unit span along the blade obtained using the pseudo-spectral LES solver. The values of the relative error of axial force at $r/R \leq 0.16$ in (a) are set as zero since the axial force therein is negligible small.

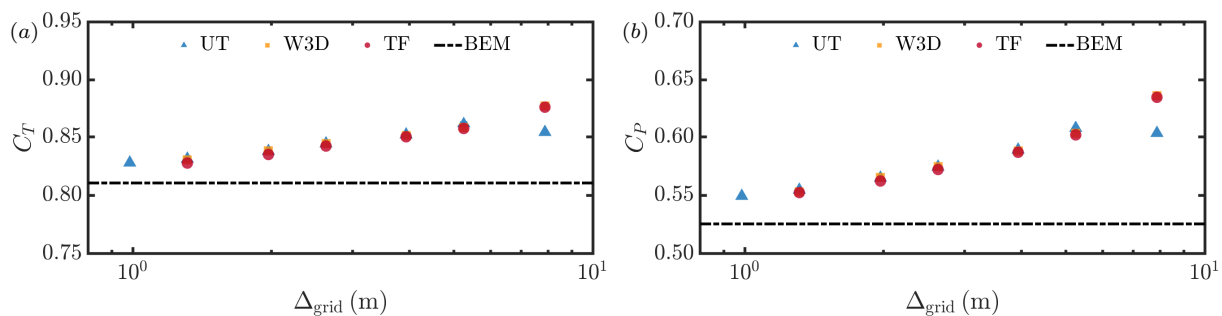


FIGURE 6 The (a) thrust C_T and (b) power C_P coefficient of the NREL 5 MW wind turbine as function of the employed grid resolutions Δ_{grid} . The dashed line indicates the high-resolution ($N = 1024$) BEM reference results and the symbols the simulation results, see table 2 for details.

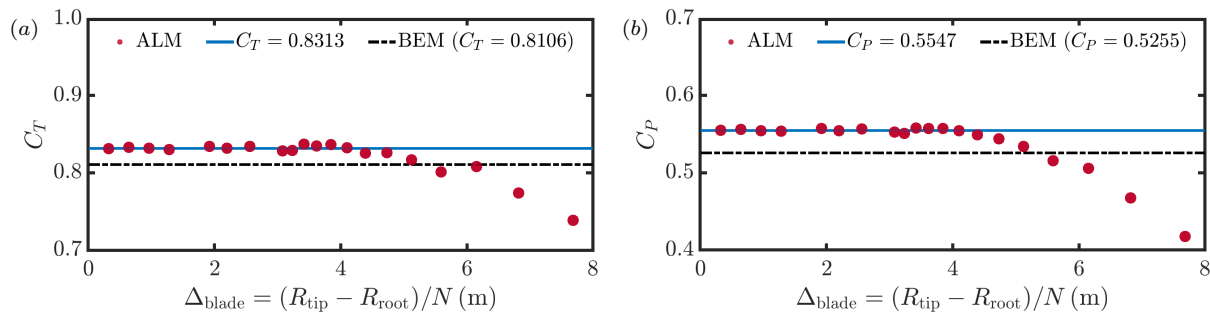


FIGURE 7 The (a) thrust C_T and (b) power C_P coefficient as function of the distance between the actuator points Δ_{blade} for the simulation cases with $\Delta_{\text{grid}} = 1.31$ meters, see in table 3, versus the high-resolution BEM results.

5 Conclusions

We compared actuator line model (ALM) approach for the NREL 5 MW wind turbine in uniform inflow using three large eddy simulations codes with results from blade element momentum (BEM) theory. The results from the three codes agree within 1% for grid resolution $\Delta_{\text{grid}} \leq 5.25$ m, which provides cross-validation of the ALM implementations. The ALM results converge towards BEM without the need for tip correction with increasing grid resolution and for $\Delta_{\text{grid}} = 0.98$ m the difference between the power and thrust coefficient obtained using ALM and BEM is 4.5% and 2.1%, respectively. We note that ALM results are not expected to fully converge towards BEM theory as both methods are slightly different, for example, due to the use of a force projection method in the ALM method. However, we note that the relative difference in the local axial and tangential forces along the blades obtained from ALM simulations using $\Delta_{\text{grid}} = 1.97$ m and $\Delta_{\text{grid}} = 0.98$ m can be as large as 10%, which shows that a high numerical resolution is required to capture local blade loadings accurately. We find that the accuracy of the ALM mainly depends on the employed grid spacing and that reducing the spacing between the actuator points per blade below three times the employed grid

TABLE 3 Comparison of the ALM simulations for the NREL 5 MW turbine using the pseudo-spectral LES solver with different number of actuator points N using the Gaussian projection function (5) and grid resolution $N_x \times N_y \times N_z = 768 \times 576 \times 576$.

Case	Δ_{blade} (m)	N	C_P	C_T
F	0.32	192	0.5547	0.8313
F ₉₆	0.64	96	0.5558	0.8328
F ₆₄	0.94	64	0.5546	0.8316
F ₄₈	1.28	48	0.5537	0.8300
F ₃₂	1.92	32	0.5573	0.8338
F ₂₈	2.20	28	0.5544	0.8320
F ₂₄	2.56	24	0.5566	0.8343
F ₂₀	3.08	20	0.5528	0.8285
F ₁₉	3.24	19	0.5507	0.8287
F ₁₈	3.42	18	0.5576	0.8369
F ₁₇	3.62	17	0.5575	0.8345
F ₁₆	3.84	16	0.5571	0.8365
F ₁₅	4.10	15	0.5544	0.8324
F ₁₄	4.39	14	0.5494	0.8256
F ₁₃	4.73	13	0.5440	0.8259
F ₁₂	5.12	12	0.5343	0.8165
F ₁₁	5.59	11	0.5157	0.8013
F ₁₀	6.15	10	0.5058	0.8079
F ₀₉	6.83	9	0.4673	0.7741
F ₀₈	7.69	8	0.4179	0.7386

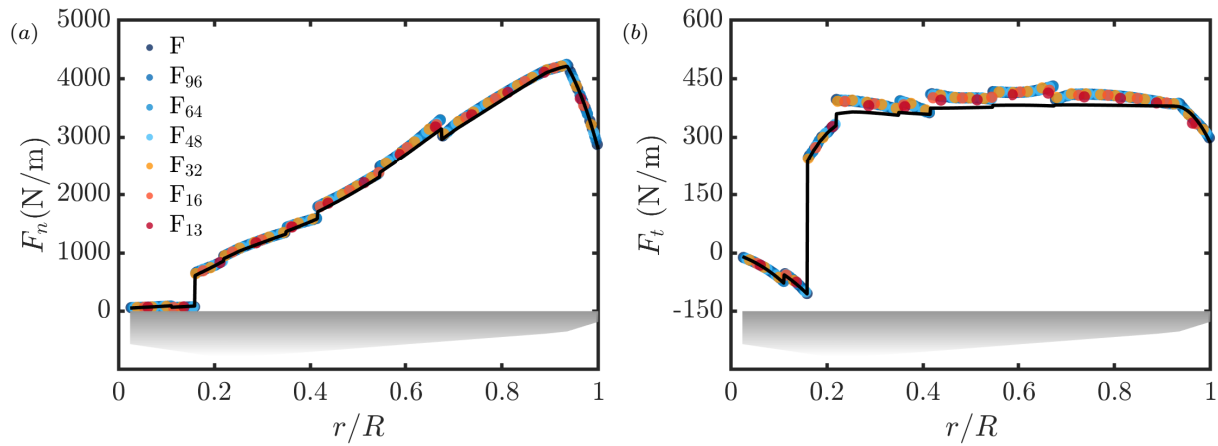


FIGURE 8 The (a) axial and (b) tangential force per unit span along the blade. The solid line indicates the high-resolution ($N = 1024$) BEM reference results. The symbols indicate the ALM simulation results obtained on grid with $\Delta_{\text{grid}} = 1.31$ meters but a varying number of actuator points, see table 3 for details.

spacing has a limited effect on the obtained accuracy due to the force project method employed in the ALM model. The insight that the number of actuator points per blade can be lower than suggested by some previous studies can be helpful to improve the efficiency of simulations in which the ALM overhead is significant. The alternative force projection method that is proposed provides another potential avenue of optimization. This can happen, for example, when simulations are performed on many cores as the ALM calculations are local in space or when the ALM model is employed to simulate the flow in wind farms with various turbines.

Acknowledgements

The work is part of the European Commission Project “High Performance Computing for Wind Energy (HPCWE)” with agreement no. 828799. This work is part of the Shell-NWO/FOM-initiative Computational sciences for energy research of Shell and Chemical Sciences, Earth, and Live Sciences, Physical Sciences, FOM, and STW. We also acknowledge the support from FAPESP (Fundação de Apoio à Pesquisa do Estado de São Paulo), Proc. 2019/01507-8, for this research. B. S. Carmo thanks the Brazilian National Council for Scientific and Technological Development (CNPq) for financial support in the form of a productivity grant, number 312951/2018-3. We acknowledge the following systems, where the simulations in this work were performed: the national e-infrastructure of SURFsara, a subsidiary of SURF corporation, the collaborative ICT organization for Dutch education and research; the Galileo at CINECA, Italy, under a grant from PRACE; the national supercomputer HPE Apollo Hawk at the High-Performance Computing Center Stuttgart (HLRS) under the grant number H2020HPCWE/33766; the SDumont supercomputer, from the National Laboratory for Scientific Computing (LNCC/MCTI, Brazil), through the CADASE project; and the NEXTGenIO system from EPCC – the University of Edinburgh, also under the HPCWE project.

References

1. Glauert H. *The Elements of Aerofoil and Airscrew Theory*. Cambridge: Cambridge University Press . 1926.
2. Rankine WJM. On the mechanical principles of the action of propellers. *Trans. Roy. Inst. Naval Arch.* 1865; 6: 13–30.
3. Froude W. On the elementary relation between pitch, slip and propulsive efficiency. *Trans. Roy. Inst. Naval Arch.* 1878; 19: 47–57.
4. Sørensen JN, Shen WZ. Numerical modeling of wind turbine wakes. *J. Fluids Eng.* 2002; 124: 393. doi: [10.1115/1.1471361](https://doi.org/10.1115/1.1471361)
5. Sørensen JN. *General Momentum Theory for Horizontal Axis Wind Turbines*. New York: Springer . 2016.
6. Dağ KO, Sørensen JN. A new tip correction for actuator line computations. *Wind Energy* 2020; 23: 148-160. doi: [10.1002/we.2419](https://doi.org/10.1002/we.2419)
7. Troldborg N, Sørensen JN, Mikkelsen R. Numerical simulations of wake characteristics of a wind turbine in uniform inflow. *Wind Energy* 2010; 13: 86-99. doi: [10.1002/we.345](https://doi.org/10.1002/we.345)
8. Stevens RJAM, Meneveau C. Flow Structure and Turbulence in Wind Farms. *Annu. Rev. Fluid Mech.* 2017; 49: 311-339. doi: [10.1146/annurev-fluid-010816-060206](https://doi.org/10.1146/annurev-fluid-010816-060206)
9. Martínez-Tossas LA, Churchfield MJ, Yilmaz AE, et al. Comparison of four large-eddy simulation research codes and effects of model coefficient and inflow turbulence in actuator-line-based wind turbine modeling. *J. Renew. Sustain. Energy* 2018; 10: 033301. doi: [10.1063/1.5004710](https://doi.org/10.1063/1.5004710)
10. Draper M, Guggeri A, Mendina M, Usera G, Campagnolo F. A Large Eddy Simulation-Actuator Line Model framework to simulate a scaled wind energy facility and its application. *J. Wind Eng. Ind. Aerodyn.* 2018; 182: 146-159. doi: [10.1016/j.jweia.2018.09.010](https://doi.org/10.1016/j.jweia.2018.09.010)
11. Porté-Agel F, Bastankhah M, Shamsoddin S. Wind-Turbine and Wind-Farm Flows: A Review. *Boundary-Layer Meteorol.* 2020; 74: 1-59. doi: [10.1007/s10546-019-00473-0](https://doi.org/10.1007/s10546-019-00473-0)
12. Mittal A, Sreenivas K, Taylor LK, Hereth L, Hilbert CB. Blade-resolved simulations of a model wind turbine: effect of temporal convergence. *Wind Energy* 2016; 19: 1761-1783. doi: [10.1002/we.1949](https://doi.org/10.1002/we.1949)
13. Santoni C, Carrasquillo K, Arenas-Navarro I, Leonardi S. Effect of tower and nacelle on the flow past a wind turbine. *Wind Energy* 2017; 20: 1927-1939. doi: [10.1002/we.2130](https://doi.org/10.1002/we.2130)
14. Grinderslev C, Sørensen NN, Horcas SG, Troldborg N, Zahle F. Wind turbines in atmospheric flow: fluid-structure interaction simulations with hybrid turbulence modeling. *Wind Energy Sci.* 2021; 6: 627-643. doi: [10.5194/wes-6-627-2021](https://doi.org/10.5194/wes-6-627-2021)
15. Ivanell S, Sørensen JN, Henningson D. Numerical Computations of Wind Turbine Wakes. In *Wind Energy*, edited by J. Peinke, P. Schaumann, and S. Barth 2007: 259-263. doi: [10.1007/978-3-540-33866-6_48](https://doi.org/10.1007/978-3-540-33866-6_48)
16. Mikkelsen R, Sørensen JN, Øye S, Troldborg N. Analysis of Power Enhancement for a Row of Wind Turbines Using the Actuator Line Technique. *J. Phys. Conf. Ser.* 2007; 75: 012044. doi: [10.1088/1742-6596/75/1/012044](https://doi.org/10.1088/1742-6596/75/1/012044)
17. Troldborg N, Larsen GC, Madsen HA, Hansen KS, Sørensen JN, Mikkelsen R. Numerical simulations of wake interaction between two wind turbines at various inflow conditions. *Wind Energy* 2011; 14: 859-876. doi: [10.1002/we.433](https://doi.org/10.1002/we.433)
18. Porté-Agel F, Wu YT, Lu H, Conzemius RJ. Large-eddy simulation of atmospheric boundary layer flow through wind turbines and wind farms. *J. Wind Eng. Ind. Aerodyn.* 2011; 99: 154-168. doi: [10.1016/j.jweia.2011.01.011](https://doi.org/10.1016/j.jweia.2011.01.011)
19. Churchfield MJ, Lee S, Moriarty PJ, et al. A Large-Eddy Simulation of Wind-Plant Aerodynamics. *50th AIAA Aerospace Sciences Meeting including the New Horizons Forum and Aerospace Exposition, 09-12 January 2012, Nashville, Tennessee* 2012; AIAA 2012-0537. doi: [10.2514/6.2012-537](https://doi.org/10.2514/6.2012-537)
20. Shives M, Crawford C. Mesh and load distribution requirements for actuator line CFD simulations. *Wind Energy* 2013; 16: 1183-1196. doi: [10.1002/we.1546](https://doi.org/10.1002/we.1546)
21. Jha PK, Churchfield MJ, Moriarty PJ, Schmitz S. Guidelines for volume force distributions within actuator line modeling of wind turbines on large-eddy simulation-type grids. *J. Sol. Energy Eng.* 2014; 136: 031003. doi: [10.1115/1.4026252](https://doi.org/10.1115/1.4026252)

22. Sørensen JN, Mikkelsen RF, Henningson DS, Ivanell S, Sarmast S, Andersen SJ. Simulation of wind turbine wakes using the actuator line technique. *Phil. Trans. R. Soc. A* 2015; 373(2035): 20140071. doi: [10.1098/rsta.2014.0071](https://doi.org/10.1098/rsta.2014.0071)
23. Abkar M, Dabiri JO. Self-similarity and flow characteristics of vertical-axis wind turbine wakes: an LES study. *Journal of Turbulence* 2017; 18(4): 373–389. doi: [10.1080/14685248.2017.1284327](https://doi.org/10.1080/14685248.2017.1284327)
24. Churchfield MJ, Schreck SJ, Martínez-Tossas LA, Meneveau C, Spalart PR. An Advanced Actuator Line Method for Wind Energy Applications and Beyond. *35th Wind Energy Symposium, AIAA SciTech* 2017; AIAA 2017-1998: 1-20. doi: [10.2514/6.2017-1998](https://doi.org/10.2514/6.2017-1998)
25. Martínez-Tossas LA, Churchfield MJ, Meneveau C. Optimal smoothing length scale for actuator line models of wind turbine blades based on Gaussian body force distribution. *Wind Energy* 2017; 20: 1083-1096. doi: [10.1002/we.2081](https://doi.org/10.1002/we.2081)
26. Ma Z, Lei L, Dowell E, Zeng P. An Experimental Study on the Actuator Line Method with Anisotropic Regularization Kernel. *Energies* 2020; 13: 977. doi: [10.3390/en13040977](https://doi.org/10.3390/en13040977)
27. Rocchio B, Ciri U, Salvetti MV, Leonardi S. Appraisal and calibration of the actuator line model for the prediction of turbulent separated wakes. *Wind Energy* 2020; 23(5): 1231–1248. doi: [10.1002/we.2483](https://doi.org/10.1002/we.2483)
28. Jonkman J, Butterfield S, Musial W, Scott G. *Definition of a 5-MW Reference Wind Turbine for Offshore System Development*. Golden, Colorado: National Renewable Energy Laboratory . 2009.
29. Viterna LA, Janetzke DC. Theoretical and experimental power from large horizontal-axis wind turbines. *DOE/NASA/20320-41* 1982: NASA-TM-82944. doi: [10.2172/6763041](https://doi.org/10.2172/6763041)
30. Du Z, Selig MS. A 3-D stall-delay model for horizontal axis wind turbine performance prediction. *ASME Wind Energy Symposium* 1998: AIAA-1998-21. doi: [10.2514/6.1998-21](https://doi.org/10.2514/6.1998-21)
31. Ning SA. AirfoilPrep.py Documentation: Release 0.1.0. *National Renewable Energy Laboratory (NREL)* 2013; Technical Report: NREL/TP-5000-58817. doi: [10.2172/1260130](https://doi.org/10.2172/1260130)
32. Martínez LA, Leonardi S, Churchfield MJ, Moriarty PJ. A comparison of Actuator disk and actuator line wind turbine models and best practices for their use. *50th AIAA Aerospace Sciences Meeting including the New Horizons Forum and Aerospace Exposition, 09-12 January 2012, Nashville, Tennessee* 2012; AIAA 2012-0900. doi: [10.2514/6.2012-900](https://doi.org/10.2514/6.2012-900)
33. Martínez-Tossas LA, Churchfield MJ, Meneveau C. Large Eddy Simulation of wind turbine wakes: detailed comparisons of two codes focusing on effects of numerics and subgrid modeling. *J. Phys. Conf. Ser.* 2015; 625: 012024. doi: [10.1088/1742-6596/625/1/012024](https://doi.org/10.1088/1742-6596/625/1/012024)
34. Sørensen P, Hansen AD, Rosas PAC. Wind models for simulation of power fluctuations from wind farms. *J. Wind Eng. Ind. Aerodyn.* 2002; 90: 1381-1402. doi: [10.1016/S0167-6105\(02\)00260-X](https://doi.org/10.1016/S0167-6105(02)00260-X)
35. Smagorinsky J. General circulation experiments with the primitive equations: I. The basic experiment. *Mon. Weather Rev.* 1963; 91(3): 99-164. doi: [10.1175/1520-0493\(1963\)091<0099:GCEWTP>2.3.CO;2](https://doi.org/10.1175/1520-0493(1963)091<0099:GCEWTP>2.3.CO;2)
36. Liu L, Stevens RJAM. Wall modeled immersed boundary method for high Reynolds number flow over complex terrain. *Comput. Fluids* 2020; 208: 104604. doi: [10.1016/j.compfluid.2020.104604](https://doi.org/10.1016/j.compfluid.2020.104604)
37. Gadde SN, Stieren A, Stevens RJAM. Large-Eddy Simulations of Stratified Atmospheric Boundary Layers: Comparison of Different Subgrid Models. *Boundary-Layer Meteorol.* 2021; 178(3): 363-382. doi: [10.1007/s10546-020-00570-5](https://doi.org/10.1007/s10546-020-00570-5)
38. Albertson JD. *Large Eddy Simulation of Land-Atmosphere Interaction*. PhD thesis. University of California, 1996.
39. Bou-Zeid E, Meneveau C, Parlange MB. A scale-dependent Lagrangian dynamic model for large eddy simulation of complex turbulent flows. *Phys. Fluids* 2005; 17: 025105. doi: [10.1063/1.1839152](https://doi.org/10.1063/1.1839152)
40. Meyers J, Meneveau C. Large eddy simulations of large wind-turbine arrays in the atmospheric boundary layer. *48th AIAA Aerospace Sciences Meeting Including the New Horizons Forum and Aerospace Exposition AIAA 2010-827 4 - 7 January 2010, Orlando, Florida* 2010: AIAA 2010-827. doi: [10.2514/6.2010-827](https://doi.org/10.2514/6.2010-827)
41. Calaf M, Meneveau C, Meyers J. Large eddy simulations of fully developed wind-turbine array boundary layers. *Phys. Fluids* 2010; 22: 015110. doi: [10.1063/1.3291077](https://doi.org/10.1063/1.3291077)
42. Stevens RJAM, Graham J, Meneveau C. A concurrent precursor inflow method for large eddy simulations and applications to finite length wind farms. *Renewable Energy* 2014; 68: 46-50. doi: [10.1016/j.renene.2014.01.024](https://doi.org/10.1016/j.renene.2014.01.024)
43. Deskos G, Laizet S, Palacios R. WInc3D: A novel framework for turbulence-resolving simulations of wind farm wake interactions. *Wind Energy* 2020; 23(3): 779-794. doi: [10.1002/we.2458](https://doi.org/10.1002/we.2458)
44. Laizet S, Lamballais E. High-order compact schemes for incompressible flows: A simple and efficient method with quasi-spectral accuracy. *J. Comput. Phys.* 2009; 228: 5989–6015. doi: [10.1016/j.jcp.2009.05.010](https://doi.org/10.1016/j.jcp.2009.05.010)
45. Laizet S, Li N. Incompact3d: A powerful tool to tackle turbulence problems with up to $O(10^5)$ computational cores. *Int. J. Numer. Meth. Fluids* 2011; 67: 1735-1757. doi: [10.1002/flid.2480](https://doi.org/10.1002/flid.2480)
46. Deskos G. *Numerical Simulations of Wind Turbine Wakes*. PhD Thesis, Imperial College London, UK. 2018.

47. Deskos G, Laizet S, Piggott MD. Turbulence-resolving simulations of wind turbine wakes. *Renewable Energy* 2019; 134: 989-1002. doi: [10.1016/j.renene.2018.11.084](https://doi.org/10.1016/j.renene.2018.11.084)
48. Weller HG, Tabor G, Jasak H, Fureby C. A tensorial approach to computational continuum mechanics using object-oriented techniques. *Computers in Physics* 1998; 12: 620-631. doi: [10.1063/1.168744](https://doi.org/10.1063/1.168744)
49. Bachant P, Goude A, Wosnik M. Actuator line modeling of vertical-axis turbines. *arXiv* 2018; 1605.01449v4.
50. Bachant P, Goude A, daa-mec, Wosnik M. turbinesFoam/turbinesFoam: v0.1.1. *Zenodo* 2019. doi: [10.5281/zenodo.3542301](https://doi.org/10.5281/zenodo.3542301)
51. Churchfield M, Lee S. NWTC design codes (SOWFA). *online* 2013; available on <http://wind.nrel.gov/designcodes/simulators/SOWFA>.
52. Onel HC, Tuncer IH. A comparative study of wake interactions between wind-aligned and yawed wind turbines using LES and actuator line models. *J. Phys. Conf. Ser.* 2021; 1618: 062009. doi: [10.1088/1742-6596/1618/6/062009](https://doi.org/10.1088/1742-6596/1618/6/062009)
53. Buhl MLJ. A new empirical relationship between thrust coefficient and induction factor for the turbulent windmill state. *Tech. Report NREL/TP-500-36834* 2005.
54. Burton T, Sharpe D, Jenkins N, Bossanyi E. *Wind Energy Handbook*. New York: John Wiley & Sons . 2001.
55. Ledoux J, Riffo S, Salomon J. Analysis of the Blade Element Momentum Theory. *arXiv* 2020; 2004.11100.
56. Lu H, Porté-Agel F. Large-eddy simulation of a very large wind farm in a stable atmospheric boundary layer. *Phys. Fluids* 2011; 23: 065101. doi: [10.1063/1.3589857](https://doi.org/10.1063/1.3589857)
57. Liu L, Stevens RJAM. Effects of atmospheric stability on the performance of a wind turbine located behind a three-dimensional hill. *Renewable Energy* 2021; 175: 926-935. doi: [10.1016/j.renene.2021.05.035](https://doi.org/10.1016/j.renene.2021.05.035)

